frontiers in Materials

ORIGINAL RESEARCH
published: 04 March 2022
doi: 10.3389/fmats.2022.844268

The Influence of Long-Term Autoclaving on the Properties of Ultra-High Performance Concrete

Hongwei Tian, Tamino Hirsch, Dietmar Stephan and Christian Lehmann*

Institute of Civil Engineering, Technische Universität Berlin, Berlin, Germany

OPEN ACCESS

Edited by:
Jiafei Jiang,
Tongji University, China

Reviewed by:
Tengfei Fu,
Fujian Agriculture and Forestry University, China
Neven Ukrainczyk,
Darmstadt University of Technology, Germany
Leo Gu Li,
Guangdong University of Technology, China

****Correspondence:***
Dietmar Stephan
stephan@tu-berlin.de

Specialty section:
This article was submitted to Structural Materials, a section of the journal Frontiers in Materials

Received: *27 December 2021*
Accepted: *08 February 2022*
Published: *04 March 2022*

Citation:
Tian H, Hirsch T, Stephan D and Lehmann C (2022) The Influence of Long-Term Autoclaving on the Properties of Ultra-High Performance Concrete. Front. Mater. 9:844268. doi: 10.3389/fmats.2022.844268

Thermal energy storage is a key component in harnessing renewable resources, compensating for the energy variations across time scales. A popular strategy for thermal energy storage is storing thermal energy in hot water tanks, which are generally made of copper, stainless steel, and vitreous enamel-lined carbon steel. However, these materials usually suffer a high production cost and short life cycle. UHPC with superior strength and durability holds the potential as a construction material for hot water tanks, which are commercially available and affordable for large-scale applications. During the charging process of hot water tanks, the UHPC structures are thus loaded by a long-term temperature-pressure load (autoclaving condition). However, the influence of long-term autoclaving on UHPC is still unclear. Therefore, the influence of long-term autoclaving at 200°C on the mechanical properties and microstructure of UHPC is studied here. The effect of the long-term autoclaving depends on the UHPC compositions. The compressive strength can stay robust owing to the accelerated formation of hydrates, while the flexural strength is vulnerable to the long-term autoclaving. Katoite, hydroxylellestadite, and scawtite are identified as the new hydrates in the autoclaved UHPC with typical components. The transformation of amorphous C-S-H into more ordered phases results in the low flexural strength and the undensified interface between the matrix and steel fibres. The partial replacement of cement by fly ash mitigates the detrimental effect of the long-term autoclaving. The incorporation of fly ash provides additional silica and increases the ratio of silica to cement, leading to more poorly crystallized C-S-H with a low Ca/Si ratio, which benefits microstructure densification and mechanical strength. The decrease of Ca/Si ratio and the increase of Al by fly ash accelerate the decomposition of katoite and hydroxylellestadite and formation of tobermorite. This study clarifies the influence of the long-term autoclaving on UHPC and provides guidance for developing an applicable and sustainable UHPC as the construction material for hot water tanks.

Keywords: ultra-high performance concrete (UHPC), autoclaving, fly ash, C-S-H, compressive and flexural strength

1 INTRODUCTION

Ultra-high performance concrete (UHPC) is an innovative and promising cementitious composite (Fehling et al., 2014). The ultra-high performance typically comprises two aspects: ultra-high durability and ultra-high mechanical properties (Richard and Cheyrezy 1995; Matte and Moranville 1999; Fehling et al., 2014). The ways to obtain this superior performance include eliminating coarse aggregate, optimizing granulometric distribution, incorporating ultra-fine components, and decreasing the water/binder ratio (Richard and Cheyrezy 1995; Arora et al., 2018; Lee et al., 2018; Arora et al., 2019). However, UHPC usually possesses a brittle fracture and poor ductility. One popular strategy to compensate for such a defect without sacrificing compressive strength is to introduce discrete fibres as reinforcement. Up to now, many types of fibres have been used in UHPC, e.g., organic fibres (Liu and Tan 2018; Pourfalah 2018; Missemer et al., 2019; Park et al., 2019), mineral fibres (Hassan and Wille 2018; Dong et al., 2019; Yonggui et al., 2020), and metallic fibres. Steel fibre is a popular type for UHPC reinforcement, and its influence on mechanical performance, which depends on many factors, such as geometry, distribution, and content, has been extensively studied (Park et al., 2012; Yoo et al., 2017; Zhang et al., 2018). In addition, the variation in matrix microstructure can also affect the bond properties between steel fibre and matrix. Compared with normal curing, short-term hydrothermal curing at 60 and 90°C can lead to the more densified microstructure and fibre-matrix interface in UHPC, exhibiting higher mechanical strength (Garas et al., 2012). However, for the UHPC exposed to elevated temperatures (fire resistance experiment), the hydration products may decompose and porosity increases, causing cracks and the degradation of bond strength between the matrix and fibres (Ahmad et al., 2019; Huang et al., 2019).

Thermal energy storage is known to play a vital role in harnessing renewable resources, especially solar energy, compensating for the sunlight variations across time scales (Alva et al., 2017). A hot water tank, which stocks thermal energy by heating or cooling the storage medium (water) for later conversion to electricity and heating or cooling applications, is a popular strategy for thermal energy storage. The water tanks are generally made of copper, stainless steel, and vitreous enamel-lined carbon steel. However, these materials have a short life cycle due to the commonly encountered corrosion and leakage. Concrete has also been used to construct such water tanks and possesses a relatively longer working life, which is commercially available and affordable for large-scale applications. Furthermore, a concrete water tank can be designed for larger capabilities and buried underground, minimizing the visual impact. However, the temperature of stored water is generally lower than 100°C, i.e., below the water boiling point, which restricts the energy storage density (the amount of energy per unit of volume or mass) and the applications of stored thermal energy (Heller 2000; Mangold 2007; Papanicolaou and Belessiotis 2009; Bauer et al., 2010). At a constant tank volume, increasing the temperature of stored water is a viable solution, which means that the concrete structure has to withstand a temperature-pressure load. UHPC with superior strength and durability has been widely used in large-span components, anti-explosive structures, and high-abrasion, high-corrosion environments, and it may fulfil the requirements for the water tank, holding potential as an alternative material for the construction of hot water pressure accumulators (Wang et al., 2012; Aldahdooh et al., 2013; Fehling et al., 2014; Wang et al., 2014; Shi et al., 2015; Tafraoui et al., 2016; Wu et al., 2018).

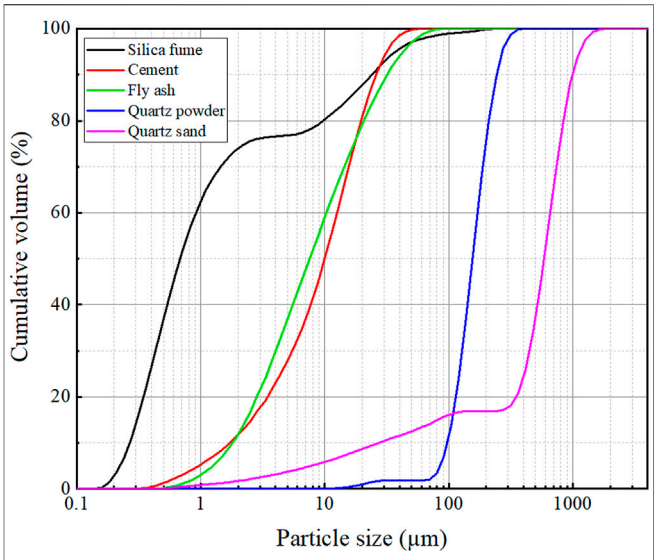

FIGURE 1 | Particle size distributions of raw materials measured by laser diffraction.

In this project, the hot water with 200°C was to be stored, and the UHPC mixtures were thus loaded by long-term autoclaving. In general, short-term hydrothermal curing is applied in prefabricated UHPC components to obtain high early strength. Such hydrothermal curing is normally with hot water/steam (60/90°C) for 24–48 h or autoclaving for several hours (Fehling et al., 2014; Zdeb 2017; Chen et al., 2018; Werder et al., 2018). However, the influence of a long period of autoclaving on the properties of UHPC is still unclear. Furthermore, supplementary cementitious materials (SCMs) are increasingly used in UHPC to compensate for the high production cost and high CO_2 emissions during Portland cement production on the one hand and to improve the concrete properties by filler effect and/or pozzolanic reaction on the other hand. In a conventional environment, the influence of SCMs is mainly determined by their physical properties, although in the long term, SCMs can chemically react and change the hydrate assemblage depending on their chemical compositions. Under autoclaving, SCMs are highly activated, and the chemical elements introduced by SCMs can exert significant influence on the hydrates' transformation and their thermal stability (Eilers et al., 1983; Colston et al., 2005; Biagioni et al., 2016).

Therefore, two mixtures, including one typical UHPC mixture and one mixture with fly ash, were investigated in the current study. After the long-term autoclaving treatment at 200°C, the samples were characterized by compressive and flexural tests, X-ray diffraction, thermogravimetric analysis, Mercury intrusion

TABLE 1 | Chemical compositions of raw materials (wt%).

	SiO_2	CaO	Al_2O_3	K_2O	MgO	Mn_2O_3	Na_2O	P_2O_5	Fe_2O_3	SO_3	TiO_2	LOI	Sum
Cement	18.85	61.16	4.85	1.07	1.74	0.06	0.22	0.07	2.83	3.62	0.22	4.92	99.61
Silica fume	98.40	0.20	0.20	0.20	0.10	-	0.15	-	0.01	0.10	-	-	99.27
Fly ash	54.25	5.56	21.03	2.08	2.36	0.09	1.05	0.98	7.98	0.30	0.92	3.29	99.89
Quartz powder	98.93	-	0.17	-	-	-	-	-	0.02	0.02	0.05	0.15	99.34

TABLE 2 | Recipes of the mixtures (mass ratio).

Mixtures	Cement	Fly ash	Silica fume	Quartz powder	Quartz sand	W/b ratio
C1	1	0	0.26	0.76	1.10	0.21
C2	0.8	0.2	0.26	0.76	1.10	0.21

porosimeter, and scanning electron microscopy to clarify the influence of long-term autoclaving.

2 MATERIALS AND METHODS

2.1 Materials

Portland cement CEM I 52.5 R complying with European standard EN 197-1 was used in this study. Quartz sand with a particle size of 0–2 mm was used as a fine aggregate. To optimize the particle size distribution and increase the packing density, silica fume and quartz powder were also introduced. The fly ash (Class F) used in this study was rich in silicon and aluminium. The particle size distributions of these materials measured with a Mastersizer 2000 (Malvern Panalytical Ltd.) are given in **Figure 1**, and the chemical compositions determined by X-ray fluorescence are shown in **Table 1**. The high performance superplasticizer of MasterGlenium ACE 430 based on a polycarboxylic ether was used to disperse the UHPC mixtures. The steel fiber used in this study had a length of 12.5 mm and a diameter of 0.2 mm.

2.2 Mixtures and Curing Regimes

The mixture recipes are shown in **Table 2** and were optimized by the modified Andreasen & Andersen packing model (Funk and Dinger 1993; Chen et al., 2019; Li et al., 2022). The water/binder (w/b) ratio was fixed at 0.21, and steel fibre content is set as 2 vol %. C1 is a typical UHPC mixture, and C2 is the blended mixture with 20 wt% fly ash replacing cement. The starting materials were first dry-mixed by a high-performance mixer (Type EL5 Eco, Maschinenfabrik Gustav Eirich GmbH and Co. KG) in the counter-current mode for 2 min. The water previously mixed with half the amount of the precalculated superplasticizer was then added, and the mixture was homogenized for 3 min in counter-current mode at a speed of 300 rpm. After a pause of 1 min, the remaining superplasticizer was added, and the mixing was restarted for another 3 min. Afterwards, the steel fiber was gradually introduced in 2 min. The mixture temperature was monitored throughout the mixing process, avoiding premature solidification caused by excessive temperature. Prismatic specimens 160·40.40 mm^3 were cast for compressive and flexural strength tests without any mechanical consolidation. For the samples prepared for microstructure characterization, quartz sand and steel fibre were eliminated. The freshly cast samples were sealed at 20 ± 2°C for 24 h, and then the hardened samples were demoulded followed by 24 h of pre-curing in water at 20 ± 2°C. One batch of samples were placed in water at 20 ± 2°C for 28 days as the reference samples. Another batch of samples were loaded by the temperature-pressure load at 200°C with saturated steam pressure 1.55 MPa for 10 days, simulating the working environment of hot water pressure accumulators. For the samples subjected to the long-term temperature-pressure load, the temperature was heated from room temperature to 200°C in ~1 h and kept for 10 days. For the microstructure analyses, after cooling to room temperature, the inner parts of samples were extracted and immersed in isopropanol for 1 day, followed by freeze-drying.

2.3 Mechanical Properties

A three-point bending test (centre-point loading) was performed on prismatic samples 40·40 160 mm^3 at a span length of 100 mm to evaluate the flexural properties. An MTS load frame was used to apply a load at a controlled displacement rate of 0.2 mm/min. The mid-span deflection of the specimen was recorded by linear variable differential transformers (LVDTs), and the average values from three samples were reported. The flexural strength can be calculated by the peak load in the load-deflection curve. The flexural toughness was evaluated by energy absorption capacity, which was calculated as the area of load versus the deflection curve up to the deflection point of 3 mm, according to ASTM C348. Compressive strength was loaded on a surface of 40·40 mm^2 of the broken samples after a flexural test at a loading rate of 2.4 kN/s, according to ASTM C349. The average value of six samples for each batch was reported as compressive strength. A statistical analysis by *t*-test was used to analyse the mechanical results, and a significance level of $p \leq 0.05$ was chosen.

2.4 X-Ray Diffraction

The mineralogical composition analysis was performed by X-ray diffraction (XRD) using an Empyrean PANalytical diffractometer with CuKα radiation (k = 1.540,598 Å). The measurements were performed at 40 kV and 40 mA in continuous mode with a resolution of 0.0131° and speed of 0.0172°/s for a 2θ range

TABLE 3 | Mechanical properties of the samples after different treatments.

Mechanical strength	Normal curing		Autoclaving	
	C1	C2	C1	C2
Compressive strength (MPa)	178.0 ± 10.1	169.9 ± 7.7	195.5 ± 11.0	218.0 ± 21.4
Flexural strength (MPa)	26.4 ± 2.5	24.0 ± 3.5	18.8 ± 2.2	26.5 ± 1.8
Energy absorption capacity (kN·mm)	15.4 ± 1.9	15.7 ± 0.4	13.2 ± 1.3	16.3 ± 0.3

from 3° to 65°. HighScore Plus software equipped with an ICSD database was used to identify the mineralogical phases.

2.5 Thermogravimetric Analysis

Thermogravimetric (TG) analysis was carried out using a TG 209 F3 Tarsus® (NETZSCH) in a nitrogen atmosphere with a 30 ml/min flow rate. 10 ± 1 mg of powder sample was used for each measurement. The temperature was increased from 20 to 1,000°C at a rate of 10°C/min.

2.6 Scanning Electron Microscope

A Zeiss Gemini SEM500 Nano VP equipped with an EDX detector was used to observe hydrates and the interface between the matrix and steel fibres. The small pieces used for SEM analysis were cut from the inner part of the UHPC samples with steel fibres. A low-viscosity epoxy resin was used to saturate the sample pieces and the surface of the hardened samples was then polished down to 1 μm using successive diamond abrasives. The chemical compositions of hydrates in autoclaved samples were measured by point element analysis. In addition, the element mapping was also conducted to study the distributions of the elements.

2.7 Mercury Intrusion Porosimetry

Due to the chemical reactions activated by the high temperature, the matrix pore structure is inevitably varied. Mercury intrusion porosimetry (MIP) using a Porotec porosimeter (Pascal 240/440) was carried out on small cubic samples. Approx. 2 g of each sample was used in the experiments under 22°C to characterize the porosity and pore size distribution. The Mercury surface tension and contact angle were assigned to 0.48 N/m and 140°, respectively. The intrusion pressure was up to 400 MPa with an increase/decrease speed of 3–7 MPa/min.

3 RESULTS AND DISCUSSION

3.1 Mechanical Properties

The compressive strength of the samples cured under different conditions is shown in **Table 3**. After normal curing for 28 days, the compressive strengths of C1 and C2 are 178.0 and 169.9 MPa, respectively. The partial replacement of cement by fly ash leads to a slight decrease in compressive strength, which is different from the influence of fly ash in normal concrete. In normal blended concrete, fly ash usually causes a low early age strength due to its low activity, while the late strength may be improved, benefiting from the pozzolanic reaction providing additional gel product (Kovács 1975; Feldman et al., 1990). However, in UHPC with a relatively low w/b ratio, cement hydration and pozzolanic reaction compete with water, and the active cement clinker phases take precedence over fly ash. Furthermore, silica fume, generally used in UHPC to optimize the particle size distribution and densify the microstructure, possesses a higher pozzolanic activity than fly ash. The pH in the liquid environment can be effectively decreased by silica fume, which also restricts the reaction of fly ash. This phenomenon is also reported in other blended UHPC mixtures (Yu et al., 2015; Zhang et al., 2017; Chang and Zheng 2020).

After the 10 days of autoclaving, the compressive strength of autoclaved C1 is 195.5 MPa, which is higher than that of normally cured C1 (t-test, $p = 0.0228$). Similarly, the autoclaved C2 also presents a higher compressive strength of 218.0 MPa than normal cured C2 (t-test, $p = 0.0057$). It is well reported that several hours of autoclaving can significantly activate the pozzolanic reaction between silica and portlandite, leading to more C-S-H being formed, which is beneficial to the mechanical properties. However, long-term autoclaving can induce the transformation of amorphous C-S-H into crystalline phases, resulting in the volume reduction of hydrates and pore coarsening (Glasser and Hong 2003; Hong and Glasser 2004; Meller et al., 2007; Kyritsis et al., 2009b). Abd Elrahman et al. reported that the compressive strength of the high performance concrete (HPC) consisting of cement (CEM I 32.5 R), quartz powder, quartz sand, and coarse aggregate is significantly decreased by long-term autoclaving (200°C) (Abd Elrahman and Hillemeier 2015). According to the experience in oil and geothermal well cementing under hydrothermal conditions, α-dicalcium silicate hydrate $Ca_2(SiO_3OH)OH$ (α-C_2SH) is usually encountered, causing microstructure degradation. To avoid this problem, additional silica (approx. 35-40 wt%) is introduced to reduce the Ca/Si ratio to approx. 1.0, leading to other C-S-H phases, such as tobermorite $Ca_5Si_6O_{16}(OH)_2{\cdot}4(H_2O)$ and xonotlite $Ca_6(Si_6O_{17})$ $(OH)_2$, depending on the temperature and effective Ca/Si ratio (Colston et al., 2005; Nelson and Guillot 2006; Kyritsis et al., 2009a). In this way, the UHPC components quartz powder and silica fume make it robust in long-term autoclaving to prevent strength degradation, although the addition of these materials initially aims to enhance the packing density and microstructure. Note that the physicochemical properties (size and crystallinity) of silica-containing materials should be considered, as the silica-containing materials with different activity can change the hydrates assemblage. For example, Krakowiak et al. (Krakowiak et al., 2018) conducted a comparative study on the crystalline α-quartz with different sizes at 200°C. It was found that gyrolite $Ca_8(Si_4O_{10})_3(OH)_4{\cdot}7H_2O$ and 11 Å tobermorite dominate in the samples containing coarser quartz, while

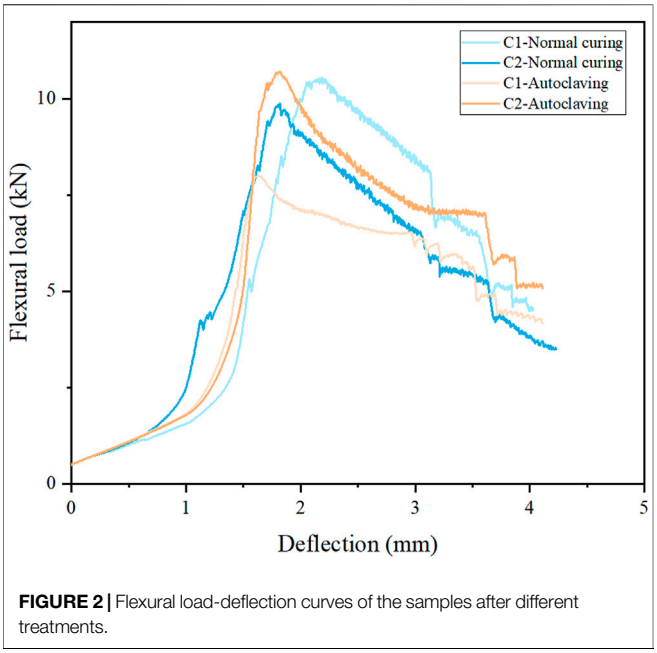

FIGURE 2 | Flexural load-deflection curves of the samples after different treatments.

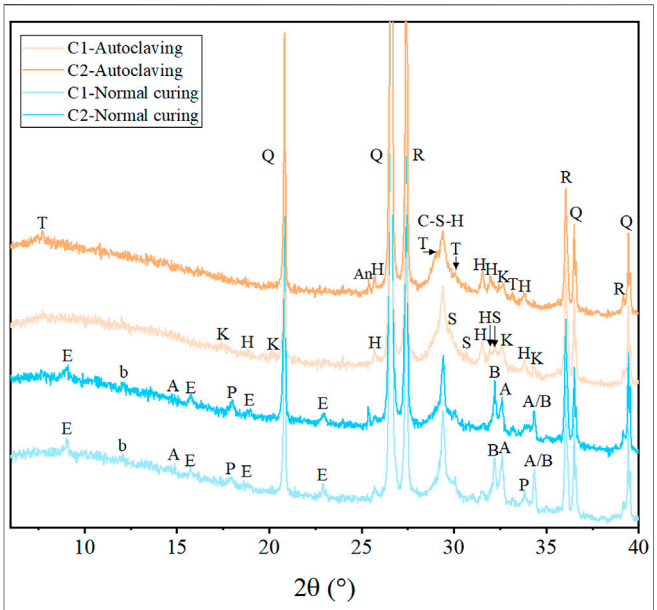

FIGURE 3 | Diffraction patterns of the samples after different treatments (Q: quartz, A: alite, B: belite, b: calcium aluminoferrite, E: ettringite, P: portlandite, T: tobermorite, S: scawtite, H: hydroxylellestadite, K: katoite, R: rutile).

poorly crystalline C-S-H predominates in the samples with fine quartz. Besides, the morphology of the hydrates can be also affected by the silica accessibility. The sample with active silica fume presents the granular xonotlite (major phase), while the sample with quartz powder generates needle-like xonotlite (major phase) accompanied by higher mechanical strength (Eilers et al., 1983).

The influence of autoclaving on sample behaviour under flexural testing is shown in **Figure 2**. After normal curing, the flexural strengths of C1 and C2 are 26.4 and 24.0 MPa, respectively, indicating that the addition of fly ash also decreases the flexural strength. However, once subjected to autoclaving, the flexural strength of autoclaved C1 significantly decreases to 18.8 MPa (t-test, p = 0.0022, compared with normally cured C1), although its compressive strength is increased by autoclaving. A similar phenomenon was also reported in (Yazıcı et al., 2009; Chen et al., 2018; Yazıcı et al., 2013), probably because the bond strength of hydrates is decreased by long-term autoclaving due to the transformation of amorphous C-S-H into more ordered phases. The energy absorption capacity was calculated to evaluate the flexural toughness as shown in **Table 3**. It can be seen that normally cured C1 and C2 present comparable energy absorption capabilities (15.4 kN·mm and 15.7 kN·mm for normally cured C1 and C2, respectively). However, the energy absorption capacity of autoclaved C1 is significantly decreased to 13.2 kN·mm, consistent with the decrease of flexural strength after autoclaving. It seems that the mixture of C1 can ensure the robust compressive strength, but cannot prevent the detrimental effect on flexural properties caused by long-term autoclaving. Krakowiak et al. reported that the strength retrogression is associated with a change of the proportions of C-S-H gel and crystalline C-S-H in the matrix (Krakowiak et al., 2015).

Interestingly, the addition of fly ash in autoclaved C2 increases the flexural strength to 24.8 MPa (t-test, p = 0.0279, compared with autoclaved C1; t-test, p = 0.3243, compared with normally cured C2), while the energy absorption capacity is also improved to 16.3 kN·mm. The results imply that the influence of long-term autoclaving on UHPC is highly related to the mixture composition. The partial replacement of cement by fly ash can mitigate the degradation of mechanical properties caused by long-term autoclaving. The similar effect was also reported in the literature (Abd Elrahman and Hillemeier 2015) that the addition of fly ash mitigates the strength degradation caused by long-term autoclaving. As the fly ash used in this study is rich in Si and Al, the partial replacement of cement by fly ash decreases the effective Ca/Si ratio in the matrix, leading to the C-S-H phases with a low Ca/Si ratio, associated with high mechanical strength. In addition to fly ash, metakaolin as a material rich in Si and Al is also studied in combination with cement and/or silica powder under hydrothermal conditions (Kuzielová 2018; Kuzielová et al., 2019). The increase of Al in the matrix can accelerate the formation of hydrogarnet. Such phase may degrade the microstructure and mechanical strength due to its high density. However, in the matrix with a low Ca/Si ratio, the addition of Al-rich materials can stabilize tobermorite at temperature above 150°C, which benefits mechanical strength (Eℓ-Hemaly et al., 1977; Biagioni et al., 2016; Chen et al., 2017). For example, the compressive strength of the Portland cement pastes is increased by the appropriate addition of metakaolin under hydrothermal conditions (Bu et al., 2016). However, the content of Al should be controlled because excessive Al, which exceeds the upper limit of the incorporation of Al into

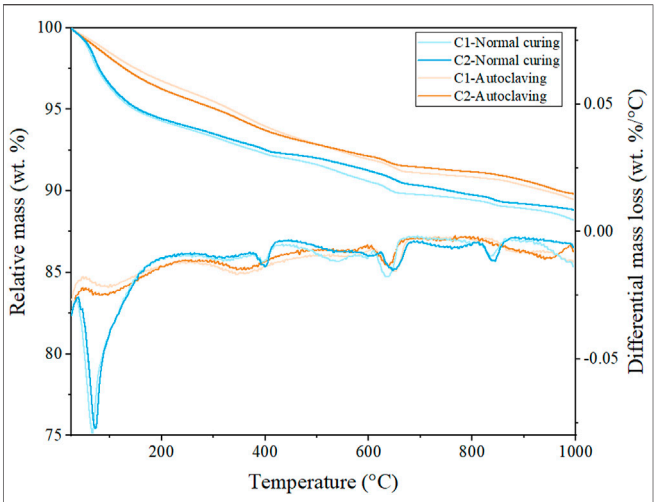

FIGURE 4 | TG and DTG diagrams of the samples after different treatments.

tobermorite, leads to the formation of hydrogarnet (Kyritsis et al., 2009a; Kyritsis et al., 2009b; Meller et al., 2009b). Therefore, the phases assemblage and microstructure are further discussed in the following sections.

3.2 XRD Analysis

The mineralogical compositions of the mixtures after different treatments are characterized by XRD, as shown in **Figure 3**. 10 wt % rutile was added as an internal standard to quantify the mineral content. However, due to the severe peak overlaps, the quantification result is unreliable and not presented here, but the rutile peaks can also work as an indicator to roughly estimate the phase evolution. For normal cured samples, the typical hydration products ettringite, portlandite, and amorphous C-S-H can be clearly identified. However, the hydrates in autoclaved samples are substantially changed. Both portlandite and ettringite disappear in autoclaved C1 and C2. Ettringite is known to be unstable at high temperatures and decompose with formation of phases like sulphate-AFm $Ca_4Al_2O_6(SO_4)\cdot 14H_2O$ and potentially bassanite $CaSO_4.0.5H_2O$, depending on the chemical composition of the matrix and the temperature-pressure conditions. At even higher temperatures, bassanite decomposes to anhydrite $CaSO_4$, and sulphate-AFm disappears, forming katoite $(Ca_3Al_2(SiO_4)_x\ (OH)_{4(3-x)};\ 0 \le x \le 3)$ and sulphate-containing phases (Vladimír and Vepek 1975; Meller et al., 2009a). In this study, the peaks of katoite are identified in both autoclaved C1 and C2, while its intensity in autoclaved C1 is stronger than that in autoclaved C2. Besides, hydroxylellestadite $Ca_{10}(SiO_4)_3(SO_4)_3(OH)_2$ as a sulphate-containing phase forms in autoclaved samples, which the sulphate originates from the decomposition of ettringite (Sauman and Vavrin 1980; Vladimír 1992).

According to the C-S-H diagrams by Taylor (Taylor 1964), Hong and Glasser (Hong and Glasser 2004), and Meller et al. (Meller et al., 2005; Meller et al. 2009b; Meller et al. 2007), the initially formed amorphous C-S-H gel converts to crystalline phases at hydrothermal conditions. The type and formation rate of newly formed crystalline phases vary with the temperature and the composition of raw materials. Scawtite $Ca_7(Si_6O_{18})\ (CO_3)\cdot 2H_2O$, which is stable at 140–300 °C (Harker 1965), is observed in autoclaved C1. According to the SEM point element analysis (**Section 3.4**), the Ca/Si ratio of the hydrates in autoclaved C1 ranges between around 1.0–2.0, consistent with the formation of scawtite. In such chemical environment, crystalline C-S-H xonotlite is usually encountered at 200°C (Hong and Glasser 2004). However, there is no apparent signal of xonotlite identified in autoclaved C1, probably because the carbonation transforms xonotlite to scawtite (Nelson 1979; Eilers et al., 1983; Grabowski and Gillott 1989) and the densified UHPC matrix restricts the crystallization of xonotlite which is discussed later. It is reported that scawtite can strongly affect the matrix performance and cause brittleness (Berger 1979; Eilers et al., 1983). This may contribute to the low flexural strength of autoclaved C1.

Tobermorite as the only crystalline C-S-H phase is identified in autoclaved C2. The partial replacement of cement by Si-rich fly ash increases the ratio of silica to cement, leading to a reduced Ca/Si ratio, which favours tobermorite formation in autoclaved C2. This effect is further confirmed by SEM analysis in **Section 3.4**. Due to the reduced Ca/Si ratio in autoclaved C2, katoite decomposes as an important intermediate of tobermorite, which coincides with the result that the peaks of katoite in autoclaved C2 are weaker than that in autoclaved C1. Another intermediate of tobermorite under hydrothermal conditions is hydroxylellestadite (Matsui et al., 2011). Accordingly, anhydrite as a decomposition product of hydroxylellestadite is identified in autoclaved C2, indicating the transformation of hydroxylellestadite to tobermorite. Furthermore, the addition of fly ash increases the Al content in the matrix (see **Section 3.4**), and the incorporation of Al into tobermorite can improve its thermal stability, preventing the conversion of tobermorite to xonotlite and scawtite under long-term autoclaving (Shaw et al., 2000a; Hong and Glasser 2004). Compared with scawtite, katoite, and hydroxylellestadite, tobermorite has a low density and thus a high solid volume. The transformation of katoite and hydroxylellestadite to tobermorite and the prevention of tobermorite to scawtite densify the UHPC microstructure, benefiting the high mechanical strength of autoclaved C2. The benefiting effect of tobermorite on microstructure and mechanical strength is also confirmed in the fabrication of calcium silicate boards (Chen et al., 2017; Wang et al., 2019), autoclaved aerated concrete (Mitsuda et al., 1992; Shams et al., 2021), and well cementing (Nelson and Guillot 2006).

Except for the crystalline phases in autoclaved C1 and C2, a diffuse peak at ~29.4° 2θ is observed, indicating that the poorly crystallized C-S-H remains until the end of autoclaving without conversion to crystalline phases. The XRD peak broadening mainly originates from the small crystallite size and a low-ordered crystal structure (Young 2002). This phenomenon of poorly crystallized C-S-H remaining after autoclaving is also observed in the literature (Matsui et al., 2011; Krakowiak et al., 2018), which has two explanations. The high solid volume fraction of the matrix provides limited space for crystallization and restricts the transformation of poorly

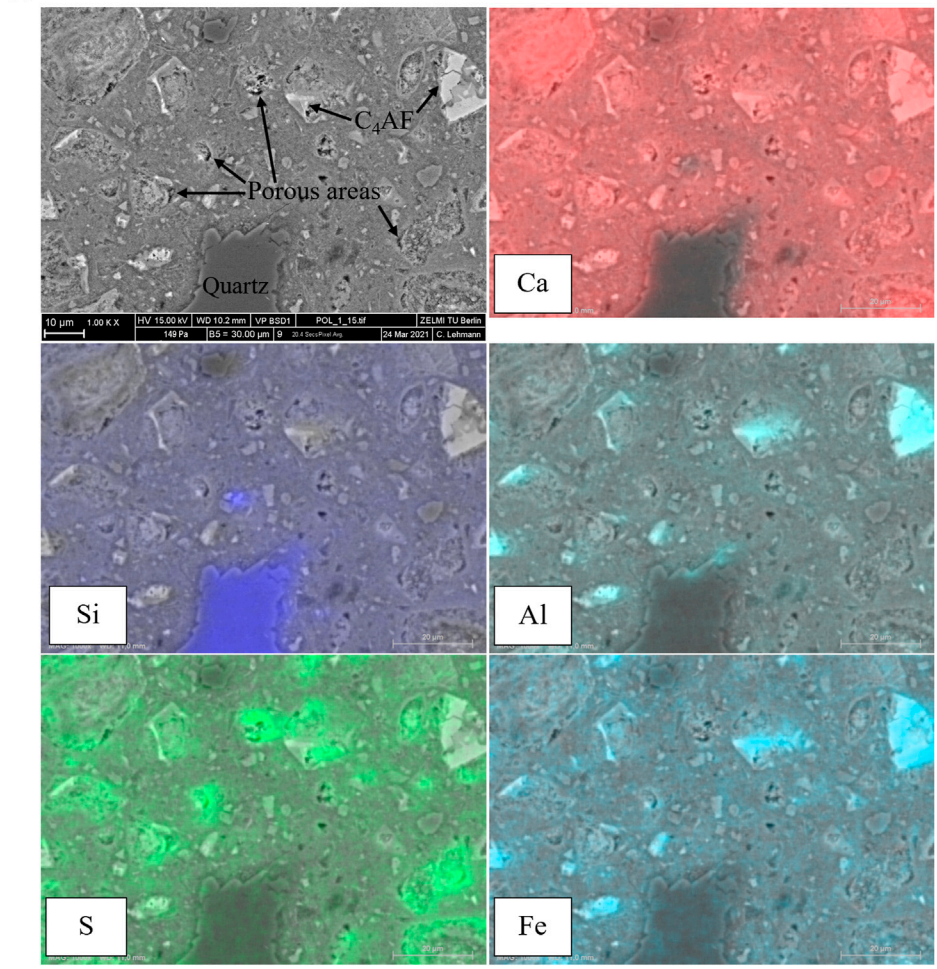

FIGURE 5 | Element mapping of the autoclaved C1 **(A)** and C2 **(B)**.

crystallized C-S-H into crystalline phases. Besides, the C-S-H precursor with Ca/Si < 1 contains long and cross-linked chains of silicate tetrahedra, which is relatively hard to transform into crystalline phases, as a larger number of bonds need to be reorganized compared to the C-S-H precursor with Ca/Si > 1 (Chen et al., 2004; Nonat 2004; Richardson 2004). In this study, the UHPC mixtures have a low w/b ratio and the densified microstructure of matrix provides insufficient space for crystallization, suppressing the transformation of poorly crystallized C-S-H to crystalline phases in autoclaved C1 and C2. This effect is infrequent in other hydrothermal conditions which the mixtures possess relatively higher w/b ratios (Abd Elrahman and Hillemeier 2015; Cheng et al., 2021). Furthermore, in autoclaved C2, the partial replacement of cement by fly ash decreases the Ca/Si ratio of the matrix and thus leads to the formation of C-S-H precursor with a low Ca/Si ratio which has less convertibility to crystalline phases. Therefore, compared with autoclaved C1, more poorly crystallized C-S-H is maintained in autoclaved C2, without conversion to crystalline phases, which strengthens the bond property and provides higher flexural strength. This effect is further discussed in **Section 3.3** and **Section 3.4** , considering the results of TG and SEM analysis.

3.3 TG Analysis

TG and DTG diagrams of the samples after different curing treatments are shown in **Figure 4**. For normally cured samples, the first peak up to ~230°C of the differential curve corresponds to the water loss in ettringite and C-S-H gel (Myers et al., 2015; Guo et al., 2017). The following small peak from around 260–370°C belongs to the dehydroxylation of aluminium hydroxide from ettringite columns. AFm (Al_2O_3-Fe_2O_3-monophase) also loses the layer water in this temperature range (Scrivener et al., 2016). The peak centred at ~400°C is assigned to the portlandite dehydroxylation, and the carbonate decomposition occurs at ~640°C. The last peak at ~840°C is related to the dehydroxylation and recrystallization of C-S-H to wollastonite ($Ca_3Si_3O_9$). It can be seen that the partial replacement of cement by fly ash slightly decreases the hydration products of ettringite and amorphous C-S-H in normally cured C2, which leads to the

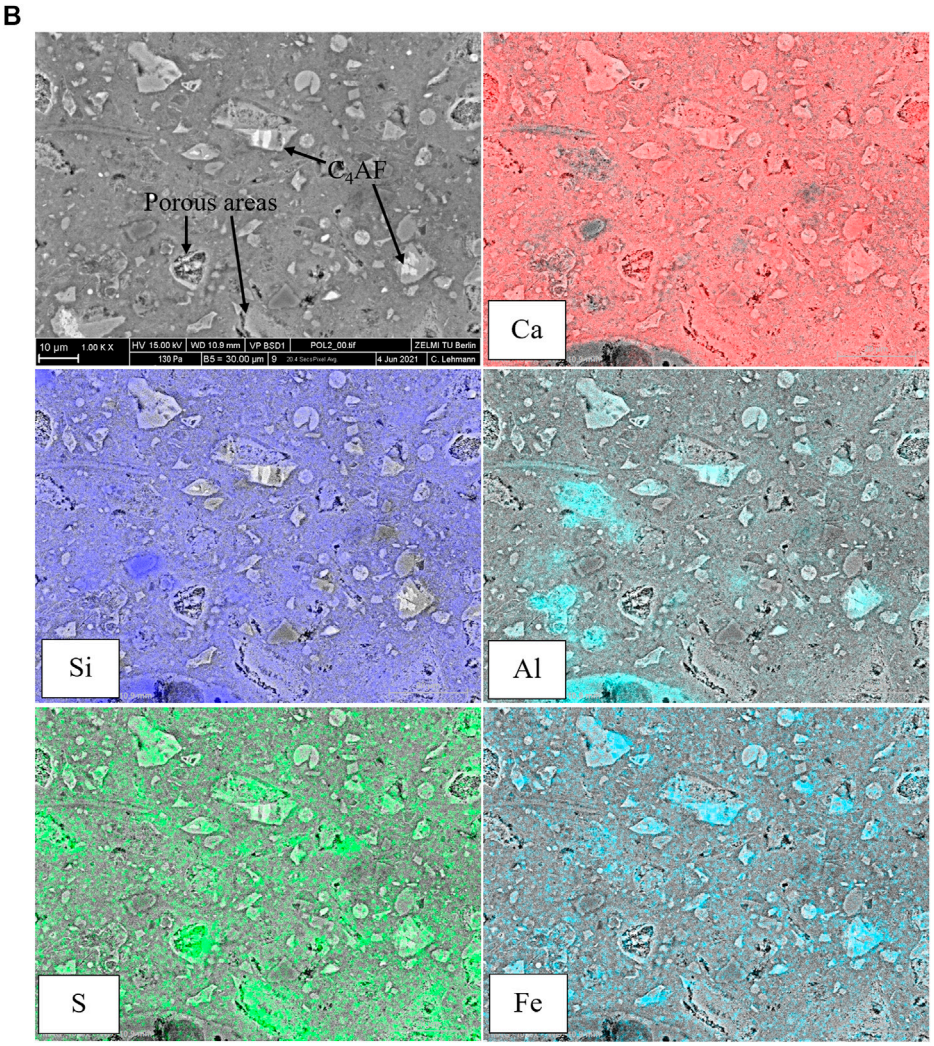

FIGURE 5 | (Continue)

relatively low mechanical strength of normally cured C2, compared with normally cured C1.

The signals of the autoclaved samples are quite different. The first water loss peak up to around 250°C significantly decreases. This is because ettringite decomposes under autoclaving condition and a part of the C-S-H gel transforms into more ordered phases, losing the excessive gel water after autoclaving. Furthermore, the water loss of autoclaved C2 in this temperature range is more significant than that of autoclaved C1. This is consistent with the discussion in **Section 3.2** that due to the partial replacement of cement by fly ash, more poorly crystallized C-S-H with a low Ca/Si ratio remains in autoclaved C2, providing more loosely bound water. It is reported that the fracture toughness is positively related to the specific surface area of the solid building blocks of the matrix (Krakowiak et al., 2015). The maintenance of a higher amount of poorly crystallized C-S-H in autoclaved C2 provides a higher specific surface area, leading to the enhanced flexural properties. Besides, tobermorite formed in autoclaved C2 loses its four interlayer water molecules per formula unit between 50 and 250°C (Shaw et al., 2000b; Biagioni et al., 2016). The addition of fly ash increases the Al content in matrix, and the uptake of Al in C-S-H is thus accelerated, which may also increase the water content in C-(A-)S-H (Gartner et al., 2017). The sharp peak of portlandite dehydroxylation is not observed in autoclaved samples. Instead, a broad and flat peak from 250 to 600°C appears in both autoclaved C1 and C2. It is reported that the remaining molecular water of tobermorite (except the preceding four loosely bound water molecules) is lost in this temperature range (dehydroxylation process) (Shaw et al., 2000b; Biagioni et al., 2016). However, katoite decomposes at above 260°C (Rivas-Mercury et al., 2008), and scawtite decomposes at around 400°C (Marincea et al., 2001). Therefore, for autoclaved C1, the water loss from 250 to 600°C is mainly contributed by the decomposition of katoite and scawtite, while for autoclaved C2, the water loss in this temperature range mainly originates

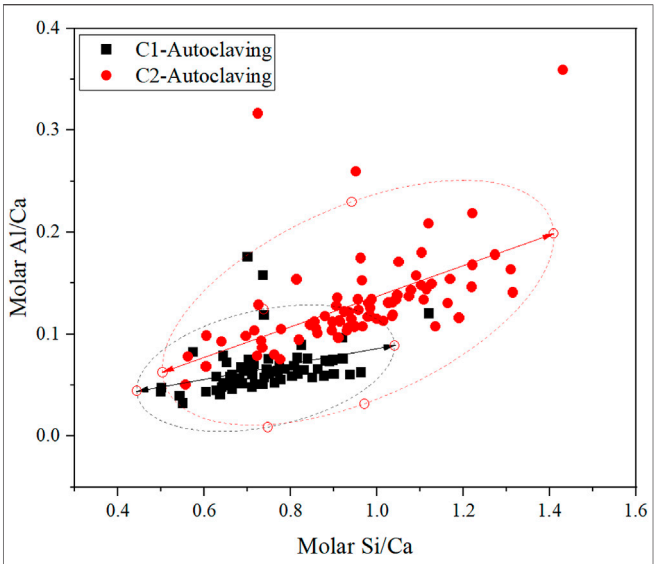

FIGURE 6 | Point element analysis of the hydrates in autoclaved samples (fitting result at 95% confidence level).

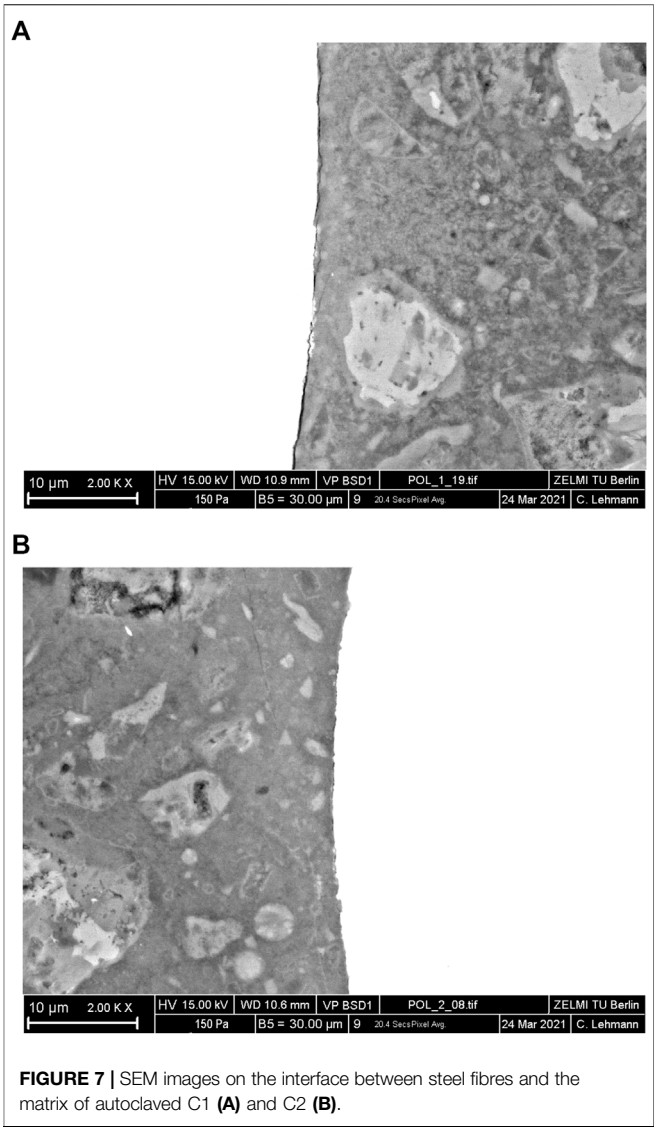

FIGURE 7 | SEM images on the interface between steel fibres and the matrix of autoclaved C1 **(A)** and C2 **(B)**.

from the dehydroxylation of tobermorite. Interestingly, compared with autoclaved C2, autoclaved C1 presents a higher mass loss at ~640°C, which is probably due to the more calcite being decomposed from scawtite. The last broad peak from ~800°C to the end of heating is assigned to the C-S-H dehydroxylation in autoclaved C1 and C2, for which the temperature is higher than that in normally cured C1 and C2. Due to the pozzolanic reaction, the C-S-H formed in autoclaved samples possesses a lower Ca/Si ratio characterized by higher polymerization degree and longer silicate chains, requiring more energy to dehydroxylate and reorganize into wollastonite (Chen et al., 2004; Nonat 2004; Richardson 2004).

3.4 SEM Analysis

To further clarify the influence of the long-term autoclaving on UHPC, SEM element mapping is carried out. For autoclaved C1 (**Figure 5A**), a quartz particle with a blurred surface is observed, which is also reported in oil well cement systems (Palou et al., 2013; Krakowiak et al., 2015) and other kinds of cementitious products treated by hydrothermal curing (Peters et al., 1978; Rashad et al., 2012). Silica reactivity is proportional to its available surface area and crystallinity (Eilers and Nelson 1979; Matsui et al., 2011; Krakowiak et al., 2018). The presence of silica with high reactivity, e.g., silica fume, restricts the reaction of silica with low reactivity, e.g., quartz powder. In this study, the highly reacted surface of quartz particles indicates that the silica fume in UHPC probably has been exhausted by the active pozzolanic reaction under the long-term autoclaving.

On the other hand, some calcium aluminoferrite particles (marked as C_4AF) remain unhydrated after the long-term autoclaving, while no silicate clinker is observed, as confirmed by the XRD results. Due to the low w/b ratio in UHPC, cement hardly hydrates entirely at room temperature. However, during the long-term autoclaving, excessive gel water is released through the transformation of amorphous C-S-H into more ordered phases, and the clinker hydration can thus achieve a higher degree, compared with the normally cured samples. Aluminoferrite phase generally has fast kinetics under early hydration once in contact with water. Calcium sulphates, e.g., anhydrite and gypsum, can suppress its hydration, which are used to prevent premature stiffening. Possible suppression mechanisms are the adsorption of sulphate ions at active dissolution sites and the formation of sulphate-AFm around anhydrous particles (Ectors et al., 2013; Morin et al., 2017). In this study, sulphate-AFm is unstable under the long-term autoclaving condition, while a large amount of S still concentrates around the ferrite particles, as shown in S mapping (**Figure 5A**), which indicates that rather than sulphate-AFm, the newly formed sulphate-containing phase under the long-term autoclaving hinders the hydration of aluminoferrite phase. Furthermore, the retardation of aluminoferrite phase after heat curing is also reported in the literature (Yang and Sharp 2001), and a higher temperature exerts stronger retardation effect (20–100°C).

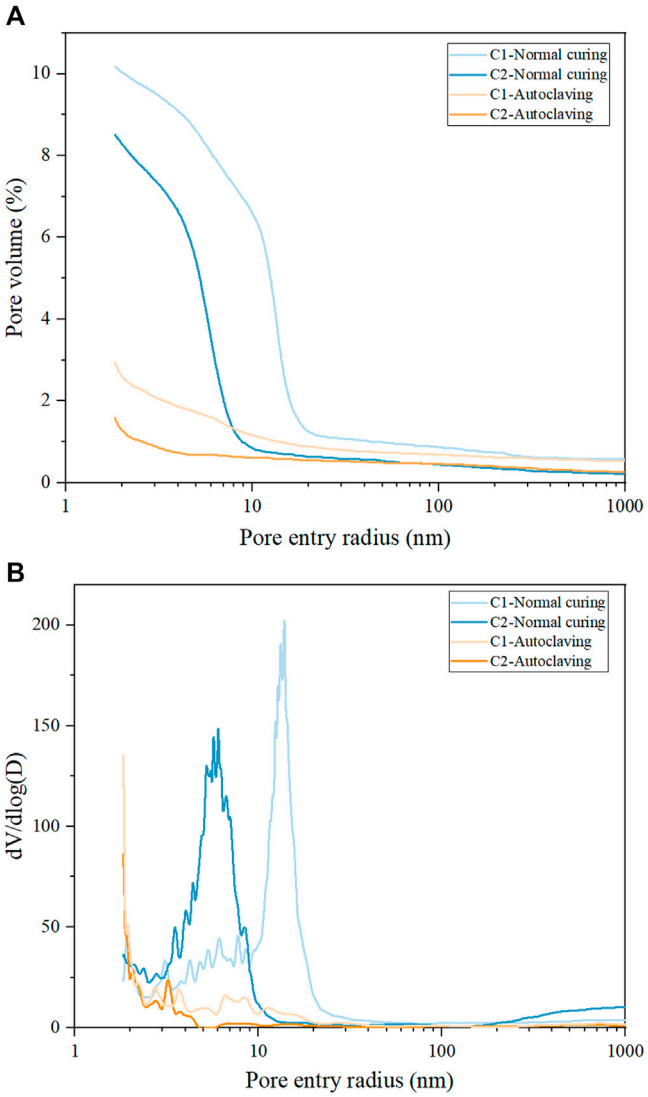

FIGURE 8 | Cumulative intrusion curves **(A)** and pore size distributions **(B)** obtained on the samples after different treatments.

Except for the aforementioned S concentrated around aluminoferrite particles, some S also accumulates in the areas that are initially occupied by other clinker phases and/or hydrates and then filled by the sulphate-containing phase, as shown in **Figure 5A**. According to the XRD results, the crystalline sulphate-containing phase is identified as hydroxylellestadite. However, it is reported that sulphate can be co-sorbed on the surface and interlayer of poorly crystallized C-S-H together with Ca^{2+} (Barbarulo et al., 2007) and inserted into the structure of crystalline C-S-H under hydrothermal conditions (Mostafa et al., 2009). Therefore, the sulphate-containing phase observed in S mapping could be a mixture of hydroxylellestadite and C-S-H incorporated with sulphate. Note that the areas filled by the sulphate-containing phase seem porous and leaky, which is probably due to the high density (low solid volume) of crystalline hydroxylellestadite. Thus, the persistence of hydroxylellestadite in autoclaved C1 may contribute to the low mechanical strength, compared with autoclaved C2. As for Al mapping (**Figure 5A**), Al widely distributes in the matrix in addition to the part concentrated around aluminoferrite particles. This is because Al can also incorporate into C-S-H, and hydrothermal curing accelerates the incorporation (Andersen et al., 2006; Jupe et al., 2008; Matsui et al., 2011). Therefore, the widely distributed Al in the matrix mainly originates from the C-(A-)S-H and katoite (decomposition product of ettringite).

Unreacted aluminoferrite particles are also observed in autoclaved C2 (**Figure 5B**). According to S mapping, the sulphate-containing phase is again observed in autoclaved C2. Similarly, due to the high density (low solid volume) of hydroxylellestadite, the areas occupied by the sulphate-containing phase present porous and leaky. However, the partial replacement of cement by fly ash decreases the content of sulphate, suppressing the formation of hydroxylellestadite. This effect benefits the microstructure densification and thus the high

mechanical strength. Besides, the transformation of hydroxylellestadite together with silica to tobermorite increases the solid volume as tobermorite has a relatively low density, which also contributes to the high mechanical strength of autoclaved C2.

Element point analysis on the autoclaved samples is further conducted, as shown in **Figure 6**. The Si/Ca ratio of hydrates in autoclaved C1 ranges between around 0.5–1.0, consistent with the formation of scawtite as discussed in **Section 3.2**. The partial replacement of cement by fly ash increases the Si/Ca ratio in autoclaved C2, originating from the increased ratio of silica to cement and the introduced Si by fly ash. Compared with autoclaved C1, autoclaved C2 can thus generate the C-S-H precursor with a higher Si/Ca ratio, which has lower convertibility to crystalline phases. Therefore, more poorly crystallized C-S-H with a high Si/Ca ratio can persist in autoclaved C2 after the long-term autoclaving, improving the microstructure and mechanical strength. Note that the Si/Ca ratio of the tobermorite solid solution is between 1.2 and 1.5 (Biagioni et al., 2015), consistent with the increased Si/Ca ratio of autoclaved C2 as shown in **Figure 6**. Besides, compared with autoclaved C1, the Al/Ca ratio of autoclaved C2 is also increased, indicating that the Al-rich fly ash can actively participate in the hydrates formation.

The interface between steel fibres and matrix was further observed, as shown in **Figure 7**. A clear interstice appears between the steel fibres and matrix in autoclaved C1 (**Figure 7A**). XRD and TG results confirmed that the C-S-H gel converts to more ordered phases, losing the excessive gel water and resulting in solid volume shrinkage. Furthermore, more katoite and scawtite formation in autoclaved C1 also contributes to the decrease of solid volume, which leads to the undensified interface between steel fibres and matrix. However, autoclaved C2 presents a denser interface between steel fibres and matrix (**Figure 7B**). This is because more poorly crystallized C-S-H with a low Ca/Si ratio remains in autoclaved C2, mitigating the degradation of matrix bonding and the solid volume shrinkage. Besides, the formation of Al-stabilized tobermorite through the decomposition of hydroxylellestadite and katoite in autoclaved C2 can increase the solid volume, which benefits the microstructure densification.

3.5 Pore Structure Analysis

The cumulative porosity curves and pore size distributions of the samples after different treatments are shown in **Figure 8**. Compared with normally cured samples, the porosities of autoclaved C1 and C2 are significantly decreased by the long-term autoclaving (**Figure 8A**). According to the literature (Matsui et al., 2011; Krakowiak et al., 2018), large crystals with a high density and crystallinity are usually observed in the mixtures with a high w/b ratio and low solid volume fraction after hydrothermal treatment, accompanied by the reported pore coarsening phenomenon. In this study, the transformation of amorphous C-S-H to crystalline phases is also confirmed. However, in the UHPC with a quite low w/b ratio and dense microstructure, the limited space suppresses the crystallization, leading to poorly crystallized C-S-H without conversion to crystalline phases. Furthermore, the typical UHPC components silica fume and quartz powder are further activated by the long-term autoclaving, generating additional C-S-H, filling the porosity, and densifying the microstructure. Therefore, compared with the normally cured samples, the critical pore entry radii of autoclaved C1 and C2 are also shifted to lower values, as shown in the curves of pore size distribution (**Figure 8B**). However, this phenomenon is not observed in other hydrothermally cured mixtures with relatively higher w/b ratios, such as that the porosities and gel pores of the blended cement pastes with metakaolin, fly ash, or silica fume increase after hydrothermal curing (150/165/200°C) (Kuzielová et al., 2017; Kuzielová 2018). The quite low w/b ratio and the high amount of silica component favors the microstructure densification of UHPC after long-term autoclaving.

Interestingly, the porosity of autoclaved C2 is lower than that of autoclaved C1. According to the pore size distribution curve, the pore volume of autoclaved C2 is dominated by gel porosity, assuming 10 nm as the dividing value between gel and capillary pores (Berodier and Scrivener 2015; Durdziński et al., 2017). As confirmed by SEM, the partial replacement of cement by fly ash provides additional Si and increases the ratio of silica to cement, resulting in more poorly crystallized C-S-H with Ca/Si < 1. This kind of C-S-H is hard to transform into crystalline phases under autoclaving, which provides more solid volume and prevents the increase of porosity. Therefore, gel pores dominate in the microstructure of autoclaved C2, which mainly originates from the fine internal porosity of hydrates. However, compared with autoclaved C2, a larger fraction of the pores from 3 to 40 nm is shown in the differential curve of autoclaved C1. This part of pores contains gel and capillary porosity, probably because more crystalline hydrates of scawtite, hydroxylellestadite, and katoite form in autoclaved C1, leading to the shrinkage of solid volume.

It is interesting to point out that there is no strict correlation between porosity and mechanical strength for the UHPC under the long-term autoclaving. Compared with normally cured C1, the porosity of autoclaved C1 is significantly decreased, but the flexural strength of autoclaved C1 is far lower than that of normal cured C1. It seems that the type of hydrates can strongly affect the flexural strength. Under the long-term autoclaving, amorphous C-S-H with high bond strength converts to more ordered phases accompanied by bond degradation. This is further confirmed by the result that more poorly crystallized C-S-H is maintained in autoclaved C2 and autoclaved C2 thus presents high flexural strength. However, the compressive strength of autoclaved C1 and C2 can stay robust under the long-term autoclaving. Compared with normally cured C1 and C2, more hydrate formation in autoclaved C1 and C2 builds the solid skeleton, benefiting the compressive strength. Compared with autoclaved C1, the persistence of more poorly crystallized C-S-H with low Ca/Si and tobermorite in autoclaved C2 ensures the higher compressive strength.

4 CONCLUSION

The influence of long-term autoclaving at 200°C with saturated pressure on the mechanical properties and microstructure of UHPC was studied. For the UHPC with typical components (silica fume, cement, quartz powder and quartz sand), the compressive strength of autoclaved C1 is increased by long-

term autoclaving, compared with that of normally cured C1. However, the flexural strength of autoclaved C1 is significantly decreased. The transformation of amorphous C-S-H to more ordered phases and the formation of katoite and hydroxylellestadite degrades the microstructure, leading to the reduced flexural strength and undensified interface between steel fibres and matrix. However, compared with normally cured C1, autoclaved C1 presents a finer texture and lower porosity, benefiting from the quite low w/b ratio and high amount of silica. Therefore, it is concluded that there is no strict correlation between the porosity and flexural strength of UHPC under long-term autoclaving, and the effect of hydrates assemblage outweighs that of porosity concerning flexural strength.

The partial replacement of cement by fly ash ensures autoclaved C2 superior compressive and flexural strength. The incorporation of fly ash increases the ratio of silica to cement, leading to more poorly crystallized C-S-H with a low Ca/Si ratio. The addition of fly ash also provides additional Al, which accelerates and stabilizes tobermorite at the expense of katoite and hydroxylellestadite under long-term autoclaving. The maintenance of poorly crystallized C-S-H (without conversion to crystalline phases) and the formation of tobermorite contribute to the densified microstructure and the enhanced mechanical strength of autoclaved C2. Autoclaved C2 thus presents a lower porosity and finer texture than autoclaved C1.

The influence of long-term autoclaving is highly related to the UHPC compositions. Due to the quite low w/b ratio and the typical components of silica fume and quartz powder, the compressive strength of UHPC can stay robust under long-term autoclaving, but exceptional attention should be paid to flexural properties. For designing UHPC working under autoclaving, the accelerated hydrothermal reactions by autoclaving should also be considered, as the traditional design rules are mainly based on the physical properties of the raw materials, aiming at a compact packing. Given the appropriate flowability, a low w/b ratio or high solid volume fraction is preferred to restrict the C-S-H transformation to crystalline phases. Additional silica, probably silica-rich SCMs of silica fume or fly ash, may be needed to maintain the poorly crystallized C-S-H with a low Ca/Si ratio under autoclaving. As for future research, permeability as an important indicator of durability is of particular concern and could be a complicated topic as the transportation of water and gas under autoclaving is quite different from that under normal conditions.

DATA AVAILABILITY STATEMENT

The original contributions presented in the study are included in the article/Supplementary Material, further inquiries can be directed to the corresponding author.

AUTHOR CONTRIBUTIONS

HT conceived and performed the experiments and wrote the manuscript. All authors participated in discussion of the research and contributed to the manuscript revision.

FUNDING

The authors acknowledge the financial support from the German Federal Ministry of Economic Affairs and Energy (No. 03ET1537A).

ACKNOWLEDGMENTS

We acknowledge support by the German Research Foundation and the Open Access Publication Fund of TU Berlin.

REFERENCES

Abd Elrahman, M., and Hillemeier, B. (2015). Influence of Hydrothermal Conditions with 200°C and 15.5bars on the Properties of Hardened HPC. *Construction Building Mater.* 85, 38–48. doi:10.1016/j.conbuildmat.2015.03.027

Ahmad, S., Rasul, M., Adekunle, S. K., Al-Dulaijan, S. U., Maslehuddin, M., and Ali, S. I. (2019). Mechanical Properties of Steel Fiber-Reinforced UHPC Mixtures Exposed to Elevated Temperature: Effects of Exposure Duration and Fiber Content. *Composites B: Eng.* 168, 291–301. doi:10.1016/j.compositesb.2018.12.083

Aldahdooh, M. A. A., Muhamad Bunnori, N., and Megat Johari, M. A. (2013). Development of green Ultra-high Performance Fiber Reinforced concrete Containing Ultrafine palm Oil Fuel Ash. *Construction Building Mater.* 48, 379–389. doi:10.1016/j.conbuildmat.2013.07.007

Alva, G., Liu, L., Huang, X., and Fang, G. (2017). Thermal Energy Storage Materials and Systems for Solar Energy Applications. *Renew. Sustain. Energ. Rev.* 68, 693–706. doi:10.1016/j.rser.2016.10.021

Andersen, M. D., Jakobsen, H. J., and Skibsted, J. (2006). A New Aluminium-Hydrate Species in Hydrated Portland Cements Characterized by 27Al and 29Si MAS NMR Spectroscopy. *Cement Concrete Res.* 36, 3–17. doi:10.1016/j.cemconres.2005.04.010

Arora, A., Aguayo, M., Hansen, H., Castro, C., Federspiel, E., Mobasher, B., et al. (2018). Microstructural Packing- and Rheology-Based Binder Selection and Characterization for Ultra-high Performance Concrete (UHPC). *Cement Concrete Res.* 103, 179–190. doi:10.1016/j.cemconres.2017.10.013

Arora, A., Almujaddidi, A., Kianmofrad, F., Mobasher, B., and Neithalath, N. (2019). Material Design of Economical Ultra-high Performance concrete (UHPC) and Evaluation of Their Properties. *Cement and Concrete Composites* 104, 103346. doi:10.1016/j.cemconcomp.2019.103346

Barbarulo, R., Peycelon, H., and Leclercq, S. (2007). Chemical Equilibria between C-S-H and Ettringite, at 20 and 85 °C. *Cement Concrete Res.* 37, 1176–1181. doi:10.1016/j.cemconres.2007.04.013

Bauer, D., Marx, R., Nußbicker-Lux, J., Ochs, F., Heidemann, W., and Müller-Steinhagen, H. (2010). German central Solar Heating Plants with Seasonal Heat Storage. *Solar Energy* 84, 612–623. doi:10.1016/j.solener.2009.05.013

Berger, R. L. (1979). Stabilization of Silicate Structures by Carbonation. *Cement Concrete Res.* 9, 649–651. doi:10.1016/0008-8846(79)90150-9

Berodier, E., and Scrivener, K. (2015). Evolution of Pore Structure in Blended Systems. *Cement Concrete Res.* 73, 25–35. doi:10.1016/j.cemconres.2015.02.025

Biagioni, C., Bonaccorsi, E., Lezzerini, M., and Merlino, S. (2016). Thermal Behaviour of Al-Rich Tobermorite. *ejm* 28, 23–32. doi:10.1127/ejm/2015/0027-2499

Biagioni, C., Merlino, S., and Bonaccorsi, E. (2015). The Tobermorite Supergroup: a New Nomenclature. *Mineralogical Mag.* 79, 485–495. doi:10.1180/minmag.2015.079.2.22

Bu, Y., Du, J., Guo, S., Liu, H., and Huang, C. (2016). Properties of Oil Well Cement with High Dosage of Metakaolin. *Construction Building Mater.* 112, 39–48. doi:10.1016/j.conbuildmat.2016.02.173

Chang, W., and Zheng, W. (2020). Effects of Key Parameters on Fluidity and Compressive Strength of Ultra-high Performance concrete. *Struct. Concrete* 21, 747–760. doi:10.1002/suco.201900167

Chen, J. J., Thomas, J. J., Taylor, H. F. W., and Jennings, H. M. (2004). Solubility and Structure of Calcium Silicate Hydrate. *Cement Concrete Res.* 34, 1499–1519. doi:10.1016/j.cemconres.2004.04.034

Chen, M., Lu, L., Wang, S., Zhao, P., Zhang, W., and Zhang, S. (2017). Investigation on the Formation of Tobermorite in Calcium Silicate Board and its Influence Factors under Autoclaved Curing. *Construction Building Mater.* 143, 280–288. doi:10.1016/j.conbuildmat.2017.03.143

Chen, T., Gao, X., and Ren, M. (2018). Effects of Autoclave Curing and Fly Ash on Mechanical Properties of Ultra-high Performance concrete. *Construction Building Mater.* 158, 864–872. doi:10.1016/j.conbuildmat.2017.10.074

Chen, Y., Matalkah, F., Soroushian, P., Weerasiri, R., and Balachandra, A. (2019). Optimization of Ultra-high Performance concrete, Quantification of Characteristic Features. *Cogent Eng.* 6, 1558696. doi:10.1080/23311916.2018.1558696

Cheng, X., Yang, X., Zhang, C., Gao, X., Yu, Y., Mei, K., et al. (2021). Effect of Red Mud Addition on Oil Well Cement at High Temperatures. *Adv. Cement Res.* 33, 28–38. doi:10.1680/jadcr.18.00224

Colston, S. L., Barnes, P., Jupe, A. C., Jacques, S. D. M., Hall, C., Livesey, P., et al. (2005). An *In Situ* Synchrotron Energy-Dispersive Diffraction Study of the Hydration of Oilwell Cement Systems under High Temperature/autoclave Conditions up to 130 °C. *Cement Concrete Res.* 35, 2223–2232. doi:10.1016/j.cemconres.2004.09.005

Dong, Z., Wu, G., Zhao, X.-L., Zhu, H., and Shao, X. (2019). Behaviors of Hybrid Beams Composed of Seawater Sea-Sand concrete (SWSSC) and a Prefabricated UHPC Shell Reinforced with FRP Bars. *Construction Building Mater.* 213, 32–42. doi:10.1016/j.conbuildmat.2019.04.059

Durdziński, P. T., Ben Haha, M., Zajac, M., and Scrivener, K. L. (2017). Phase Assemblage of Composite Cements. *Cement Concrete Res.* 99, 172–182. doi:10.1016/j.cemconres.2017.05.009

Ectors, D., Neubauer, J., and Goetz-Neunhoeffer, F. (2013). The Hydration of Synthetic Brownmillerite in Presence of Low Ca-Sulfate Content and Calcite Monitored by Quantitative In-Situ-XRD and Heat Flow Calorimetry. *Cement Concrete Res.* 54, 61–68. doi:10.1016/j.cemconres.2013.08.011

Eilers, L. H., and Nelson, E. B. (1979). "Effect of Silica Particle Size on Degradation of Silica Stabilized portland Cement," in SPE Oilfield and Geothermal Chemistry Symposium, Houston, Texas, 1979-01-22 (Houston, TX: Society of Petroleum Engineers). doi:10.2118/7875-MS

Eilers, L. H., Nelson, E. B., and Moran, L. K. (1983). High-temperature Cement Compositions-Pectolite, Scawtite, Truscottite, or Xonotlite: Which Do You Want? *J. Pet. Technol.* 35 (07), 1,373–1,377. doi:10.2118/9286-pa

Eℓ-Hemaly, S., Mitsuda, T., and Taylor, H. (1977). Synthesis of normal and Anomalous Tobermorites. *Cement Concrete Res.* 7, 429–438. doi:10.1016/0008-8846(77)90071-0

Fehling, E., Schmidt, M., Walraven, J. C., Leutbecher, T., and Fröhlich, S. (2014). *Ultra-high Performance concrete UHPC: Fundamentals - Design - Examples (BetonKalender)*. Berlin: Ernst & Sohn.

Feldman, R. F., Carette, G. G., and Malhotra, V. M. (1990). Studies on Mechanics of Development of Physical and Mechanical Properties of High-Volume Fly Ash-Cement Pastes. *Cement and Concrete Composites* 12, 245–251. doi:10.1016/0958-9465(90)90003-G

Funk, J. E., and Dinger, D. (1993). *Predictive Process Control of Crowded Particulate Suspensions: Applied to Ceramic Manufacturing*. Berlin, Germany: Springer Science & Business Media.

Garas, V. Y., Kurtis, K. E., and Kahn, L. F. (2012). Creep of UHPC in Tension and Compression: Effect of thermal Treatment. *Cement and Concrete Composites* 34, 493–502. doi:10.1016/j.cemconcomp.2011.12.002

Gartner, E., Maruyama, I., and Chen, J. (2017). A New Model for the C-S-H Phase Formed during the Hydration of Portland Cements. *Cement Concrete Res.* 97, 95–106. doi:10.1016/j.cemconres.2017.03.001

Glasser, F. P., and Hong, S.-Y. (2003). Thermal Treatment of C-S-H Gel at 1 Bar H2O Pressure up to 200 °C. *Cement Concrete Res.* 33 (2), 271–279. doi:10.1016/s0008-8846(02)00959-6

Grabowski, E., and Gillott, J. E. (1989). Effect of Replacement of Silica Flour with Silica Fume on Engineering Properties of Oilwell Cements at normal and Elevated Temperatures and Pressures. *Cement Concrete Res.* 19, 333–344. doi:10.1016/0008-8846(89)90023-9

Guo, X., Meng, F., and Shi, H. (2017). Microstructure and Characterization of Hydrothermal Synthesis of Al-Substituted Tobermorite. *Construction Building Mater.* 133, 253–260. doi:10.1016/j.conbuildmat.2016.12.059

Harker, R. I. (1965). Scawtite and its Synthesis. *Mineral. Mag. J. Mineral. Soc.* 34, 232–236. doi:10.1180/minmag.1965.034.268.18

Hassan, M., and Wille, K. (2018). Comparative Experimental Investigations on the Compressive Impact Behavior of Fiber-Reinforced Ultra High-Performance Concretes Using Split Hopkinson Pressure Bar. *Construction Building Mater.* 191, 398–410. doi:10.1016/j.conbuildmat.2018.10.020

Heller, A. (2000). 15 Years of R&D in central Solar Heating in Denmark. *Solar Energy* 69, 437–447. doi:10.1016/S0038-092X(00)00118-3

Hong, S.-Y., and Glasser, F. P. (2004). Phase Relations in the CaO-SiO2-H2o System to 200 °C at Saturated Steam Pressure. *Cement Concrete Res.* 34, 1529–1534. doi:10.1016/j.cemconres.2003.08.009

Huang, H., Wang, R., and Gao, X. (2019). Improvement Effect of Fiber Alignment on Resistance to Elevated Temperature of Ultra-high Performance concrete. *Composites Part B: Eng.* 177, 107454. doi:10.1016/j.compositesb.2019.107454

Jupe, A. C., Wilkinson, A. P., Luke, K., and Funkhouser, G. P. (2008). Class H Cement Hydration at 180 °C and High Pressure in the Presence of Added Silica. *Cement Concrete Res.* 38, 660–666. doi:10.1016/j.cemconres.2007.12.004

Kovács, R. (1975). Effect of the Hydration Products on the Properties of Fly-Ash Cements. *Cement Concrete Res.* 5, 73–82. doi:10.1016/0008-8846(75)90109-X

Krakowiak, K. J., Thomas, J. J., James, S., Abuhaikal, M., and Ulm, F.-J. (2018). Development of Silica-Enriched Cement-Based Materials with Improved Aging Resistance for Application in High-Temperature Environments. *Cement Concrete Res.* 105, 91–110. doi:10.1016/j.cemconres.2018.01.004

Krakowiak, K. J., Thomas, J. J., Musso, S., James, S., Akono, A.-T., and Ulm, F.-J. (2015). Nano-chemo-mechanical Signature of Conventional Oil-Well Cement Systems: Effects of Elevated Temperature and Curing Time. *Cement Concrete Res.* 67, 103–121. doi:10.1016/j.cemconres.2014.08.008

Kuzielová, E., Žemlička, M., Másilko, J., and Palou, M. T. (2019). Development of G-Oil Well Cement Phase Composition during Long Therm Hydrothermal Curing. *Geothermics* 80, 129–137. doi:10.1016/j.geothermics.2019.03.002

Kuzielová, E., Žemlička, M., Másilko, J., and Palou, M. T. (2017). Pore Structure Development of Blended G-Oil Well Cement Submitted to Hydrothermal Curing Conditions. *Geothermics* 68, 86–93. doi:10.1016/j.geothermics.2017.03.001

Kuzielová, E., Žemlička, M., Másilko, J , et al.Žemlička, M., Másilko, J., Palou, M. T. (2018). Effect of Additives on the Performance of Dyckerhoff Cement, Class G, Submitted to Simulated Hydrothermal Curing. *J. Therm. Anal. Calorim.* 133, 63–76. doi:10.1007/s10973-017-6806-2

Kyritsis, K., Hall, C., Bentz, D. P., Meller, N., and Wilson, M. A. (2009a). Relationship between Engineering Properties, Mineralogy, and Microstructure in Cement-Based Hydroceramic Materials Cured at 200°-350°C. *J. Am. Ceram. Soc.* 92, 694–701. doi:10.1111/j.1551-2916.2008.02914.x

Kyritsis, K., Meller, N., and Hall, C. (2009b). Chemistry and Morphology of Hydrogarnets Formed in Cement-Based CASH Hydroceramics Cured at 200° to 350°C. *J. Am. Ceram. Soc.* 92, 1105–1111. doi:10.1111/j.1551-2916.2009.02958.x

Lee, N. K., Koh, K. T., Kim, M. O., and Ryu, G. S. (2018). Uncovering the Role of Micro Silica in Hydration of Ultra-high Performance concrete (UHPC). *Cement Concrete Res.* 104, 68–79. doi:10.1016/j.cemconres.2017.11.002

Li, L. G., Feng, J. J., Lu, Z. C., Xie, H. Z., Xiao, B. F., Kwan, A. K. H., et al. (2022). Effects of Aggregate Bulking and Film Thicknesses on Water Permeability and Strength of Pervious concrete. *Powder Technol.* 396, 743–753. doi:10.1016/j.powtec.2021.11.019

Liu, J.-C., and Tan, K. H. (2018). Mechanism of PVA Fibers in Mitigating Explosive Spalling of Engineered Cementitious Composite at Elevated Temperature. *Cement and Concrete Composites* 93, 235–245. doi:10.1016/j.cemconcomp.2018.07.015

Mangold, D. (2007). Seasonal Storage–A German success story. *Sun & Wind Energy* 1, 48–58.

Marincea, S., Bilal, E., Verkaeren, J., Pascal, M.-L., and Fonteilles, M. (2001). Superposed Parageneses in the Spurrite-, Tilleyite-And Gehlenite-Bearing Skarns from Cornet Hill, Apuseni Mountains, Romania. *Can. Mineral.* 39 (5), 1435–1453. doi:10.2113/gscanmin.39.5.1435

Matsui, K., Kikuma, J., Tsunashima, M., Ishikawa, T., Matsuno, S.-Y., Ogawa, A., et al. (2011). *In Situ* time-resolved X-ray Diffraction of Tobermorite Formation in Autoclaved Aerated concrete: Influence of Silica Source Reactivity and Al Addition. *Cement Concrete Res.* 41, 510–519. doi:10.1016/j.cemconres.2011.01.022

Matte, V., and Moranville, M. (1999). Durability of Reactive Powder Composites: Influence of Silica Fume on the Leaching Properties of Very Low Water/binder Pastes. *Cement and Concrete Composites* 21 (1), 1–9. doi:10.1016/s0958-9465(98)00025-0

Meller, N., Hall, C., Kyritsis, K., and Giriat, G. (2007). Synthesis of Cement Based CaO-Al2O3-SiO2-H2o (CASH) Hydroceramics at 200 and 250 °C: *Ex-Situ* and *In-Situ* Diffraction. *Cement Concrete Res.* 37 (6), 823–833. doi:10.1016/j.cemconres.2007.03.006

Meller, N., Hall, C., and Phipps, J. S. (2005). A New Phase Diagram for the CaOAl2O3SiO2H2O Hydroceramic System at 200°C. *Mater. Res. Bull.* 40, 715–723. doi:10.1016/j.materresbull.2005.03.001

Meller, N., Kyritsis, K., and Hall, C. (2009a). The Hydrothermal Decomposition of Calcium Monosulfoaluminate 14-hydrate to Katoite Hydrogarnet and β-anhydrite: An *In-Situ* Synchrotron X-ray Diffraction Study. *J. Solid State. Chem.* 182, 2743–2747. doi:10.1016/j.jssc.2009.07.029

Meller, N., Kyritsis, K., and Hall, C. (2009b). The Mineralogy of the CaO-Al2O3-SiO2-H2o (CASH) Hydroceramic System from 200 to 350 °C. *Cement Concrete Res.* 39, 45–53. doi:10.1016/j.cemconres.2008.10.002

Missemer, L., Ouedraogo, E., Malecot, Y., Clergue, C., and Rogat, D. (2019). Fire Spalling of Ultra-high Performance concrete: From a Global Analysis to Microstructure Investigations. *Cement Concrete Res.* 115, 207–219. doi:10.1016/j.cemconres.2018.10.005

Mitsuda, T., Sasaki, K., and Ishida, H. (1992). Phase Evolution during Autoclaving Process of Aerated concrete. *J. Am. Ceram. Soc.* 75, 1858–1863. doi:10.1111/j.1151-2916.1992.tb07208.x

Morin, V., Termkhajornkit, P., Huet, B., and Pham, G. (2017). Impact of Quantity of Anhydrite, Water to Binder Ratio, Fineness on Kinetics and Phase Assemblage of Belite-Ye'elimite-Ferrite Cement. *Cement Concrete Res.* 99, 8–17. doi:10.1016/j.cemconres.2017.04.014

Mostafa, N. Y., Shaltout, A. A., Omar, H., and Abo-El-Enein, S. A. (2009). Hydrothermal Synthesis and Characterization of Aluminium and Sulfate Substituted 1.1nm Tobermorites. *J. Alloys Compd.* 467, 332–337. doi:10.1016/j.jallcom.2007.11.130

Myers, R. J., L'Hôpital, E., Provis, J. L., and Lothenbach, B. (2015). Effect of Temperature and Aluminium on Calcium (Alumino)silicate Hydrate Chemistry under Equilibrium Conditions. *Cement Concrete Res.* 68, 83–93. doi:10.1016/j.cemconres.2014.10.015

Nelson, E. B. (1979). Development of Geothermal-Well-Completion Systems. *Final Rep. (Doe/et/28324-9)*. Available at: https://digital.library.unt.edu/ark:/67531/metadc1103485/.

Nelson, E. B., and Guillot, D. (2006). "Well Cementing," in *Developments in Petroleum Science*. 2nd ed. (Sugar Land, Tex: Schlumberger), Vol. 28.

Nonat, A. (2004). The Structure and Stoichiometry of C-S-H. *Cement Concrete Res.* 34, 1521–1528. doi:10.1016/j.cemconres.2004.04.035

Palou, M., Živica, V., Ifka, T., Boháč, M., and Zmrzlý, M. (2013). Effect of Hydrothermal Curing on Early Hydration of G-Oil Well Cement. *J. Therm. Anal. Calorim.* 116, 597–603. doi:10.1007/s10973-013-3511-7

Papanicolaou, E., and Belessiotis, V. (2009). Transient Development of Flow and Temperature fields in an Underground thermal Storage Tank under Various Charging Modes. *Solar Energy* 83, 1161–1176. doi:10.1016/j.solener.2009.01.017

Park, J.-J., Yoo, D.-Y., Kim, S., and Kim, S.-W. (2019). Benefits of Synthetic Fibers on the Residual Mechanical Performance of UHPFRC after Exposure to ISO Standard Fire. *Cement and Concrete Composites* 104, 103401. doi:10.1016/j.cemconcomp.2019.103401

Park, S. H., Kim, D. J., Ryu, G. S., and Koh, K. T. (2012). Tensile Behavior of Ultra High Performance Hybrid Fiber Reinforced Concrete. *Cement and Concrete Composites* 34, 172–184. doi:10.1016/j.cemconcomp.2011.09.009

Peters, T., Iberg, R., and Mumenthaler, T. (1978). Comparative Study of the Use of a Quartz Poor Sand and a Pure Quartz Sand for Lime Silica Bricks and the Kinetics of the Hydrothermal Hardening Mechanism. *Cement Concrete Res.* 8, 415–424. doi:10.1016/0008-8846(78)90021-2

Pourfalah, S. (2018). Behaviour of Engineered Cementitious Composites and Hybrid Engineered Cementitious Composites at High Temperatures. *Construction Building Mater.* 158, 921–937. doi:10.1016/j.conbuildmat.2017.10.077

Rashad, A. M., Zeedan, S. R., and Hassan, H. A. (2012). A Preliminary Study of Autoclaved Alkali-Activated Slag Blended with Quartz Powder. *Construction Building Mater.* 33, 70–77. doi:10.1016/j.conbuildmat.2011.12.104

Richard, P., and Cheyrezy, M. (1995). Composition of Reactive Powder Concretes. *Cement Concrete Res.* 25 (7), 1501–1511. doi:10.1016/0008-8846(95)00144-2

Richardson, I. G. (2004). Tobermorite/jennite- and Tobermorite/calcium Hydroxide-Based Models for the Structure of C-S-H: Applicability to Hardened Pastes of Tricalcium Silicate, β-dicalcium Silicate, Portland Cement, and Blends of Portland Cement with Blast-Furnace Slag, Metakaolin, or Silica Fume. *Cement Concrete Res.* 34, 1733–1777. doi:10.1016/j.cemconres.2004.05.034

Rivas-Mercury, J. M., Pena, P., de Aza, A. H., and Turrillas, X. (2008). Dehydration of Ca3Al2(SiO4)Y(OH)4(3−y) (0. *J. Eur. Ceram. Soc.* 28, 1737–1748. doi:10.1016/j.jeurceramsoc.2007.12.038

Satava, V., and Veprek, O. (1975). Thermal Decomposition of Ettringite under Hydrothermal Conditions. *J. Am. Ceram. Soc.* 58, 357–359. doi:10.1111/j.1151-2916.1975.tb11513.x

Sauman, Z., and Vavrin, F. (1980). "Conditions of the Hydroxyl Ellestadite Formation in Mixtures Containing Calcium Sulphate," in 7th International Congress on the Chemistry of Cement ICCC, Paris, 106–110.

Scrivener, K. L., Snellings, R., and Lothenbach, B. (2016). *A Practical Guide to Microstructural Analysis of Cementitious Materials*. Boca Raton, Florida, USA: CRC Press.

Shams, T., Schober, G., Heinz, D., and Seifert, S. (2021). Production of Autoclaved Aerated concrete with Silica Raw Materials of a Higher Solubility Than Quartz Part II: Influence of Autoclaving Temperature. *Construction Building Mater.* 287, 123072. doi:10.1016/j.conbuildmat.2021.123072

Shaw, S., Clark, S. M., and Henderson, C. M. B. (2000a). Hydrothermal Formation of the Calcium Silicate Hydrates, Tobermorite (Ca5Si6O16(OH)2·4H2O) and Xonotlite (Ca6Si6O17(OH)2): an *In Situ* Synchrotron Study. *Chem. Geology.* 167, 129–140. doi:10.1016/S0009-2541(99)00205-3

Shaw, S., Henderson, C. M. B., and Komanschek, B. U. (2000b). Dehydration/recrystallization Mechanisms, Energetics, and Kinetics of Hydrated Calcium Silicate Minerals: an *In Situ* TGA/DSC and Synchrotron Radiation SAXS/WAXS Study. *Chem. Geology.* 167, 141–159. doi:10.1016/S0009-2541(99)00206-5

Shi, C., Wu, Z., Xiao, J., Wang, D., Huang, Z., and Fang, Z. (2015). A Review on Ultra High Performance concrete: Part I. Raw Materials and Mixture Design. *Construction Building Mater.* 101, 741–751. doi:10.1016/j.conbuildmat.2015.10.088

Tafraoui, A., Escadeillas, G., and Vidal, T. (2016). Durability of the Ultra High Performances Concrete Containing Metakaolin. *Construction Building Mater.* 112, 980–987. doi:10.1016/j.conbuildmat.2016.02.169

Taylor, H. F. W. (1964). *The Chemistry of Cements*. London: Academic Press.

Vladimír, Š. (1992). Hydrothermal Reactions in the System $3CaO{\cdot}SiO_2$-$CaSO_4{\cdot}2H_2O$-H_2o. *Ceramics - Silikaty* 36 (2), 105–108.

von Werder, J., Simon, S., Simon, C., Selleng, C., Fontana, P., and Meng, B. (2018). Autoclaving of Ultra-high Performance concrete (UHPC). *ce/papers* 2, 131–136. doi:10.1002/cepa.866

Wu C., Li J., and Su Y. (Editors) (2018). *Development of Ultra-high Performance Concrete against Blasts: Woodhead Publishing Series in Civil and Structural Engineering* (Sawston, UK: Woodhead Publishing).

Wang, C., Yang, C., Liu, F., Wan, C., and Pu, X. (2012). Preparation of Ultra-high Performance Concrete with Common Technology and Materials. *Cement and Concrete Composites* 34, 538–544. doi:10.1016/j.cemconcomp.2011.11.005

Wang, W., Liu, J., Agostini, F., Davy, C. A., Skoczylas, F., and Corvez, D. (2014). Durability of an Ultra High Performance Fiber Reinforced Concrete (UHPFRC) under Progressive Aging. *Cement Concrete Res.* 55, 1–13. doi:10.1016/j.cemconres.2013.09.008

Wang, Z., Ma, S., Zheng, S., Ding, J., and Wang, X. (2019). Flexural Strength and thermal Conductivity of Fiber-Reinforced Calcium Silicate Boards Prepared from Fly Ash. *J. Mater. Civil Eng.* 31, 4019140. doi:10.1061/(ASCE)MT.1943-5533.0002726

Yang, R., and Sharp, J. H. (2001). Hydration Characteristics of Portland Cement after Heat Curing: I, Degree of Hydration of the Anhydrous Cement Phases. *J. Am. Ceram. Soc.* 84, 608–614. doi:10.1111/j.1151-2916.2001.tb00707.x

Yazıcı, H., Deniz, E., and Baradan, B. (2013). The Effect of Autoclave Pressure, Temperature and Duration Time on Mechanical Properties of Reactive Powder

concrete. *Construction Building Mater.* 42, 53–63. doi:10.1016/j.conbuildmat.2013.01.003

Yazıcı, H., Yardımcı, M. Y., Aydın, S., and Karabulut, A. Ş. (2009). Mechanical Properties of Reactive Powder concrete Containing mineral Admixtures under Different Curing Regimes. *Construction Building Mater.* 23, 1223–1231. doi:10.1016/j.conbuildmat.2008.08.003

Yonggui, W., Shuaipeng, L., Hughes, P., and Yuhui, F. (2020). Mechanical Properties and Microstructure of basalt Fibre and Nano-Silica Reinforced Recycled concrete after Exposure to Elevated Temperatures. *Construction Building Mater.* 247, 118561. doi:10.1016/j.conbuildmat.2020.118561

Yoo, D.-Y., Kim, M. J., Kim, S.-W., and Park, J.-J. (2017). Development of Cost Effective Ultra-high-performance Fiber-Reinforced concrete Using Single and Hybrid Steel Fibers. *Construction Building Mater.* 150, 383–394. doi:10.1016/j.conbuildmat.2017.06.018

Young R. A. (Editor) (2002). *The Rietveld Method* (Oxford: Oxford Univ. Press), Vol. 5.

Yu, R., Spiesz, P., and Brouwers, H. J. H. (2015). Development of an Eco-Friendly Ultra-high Performance Concrete (UHPC) with Efficient Cement and mineral Admixtures Uses. *Cement and Concrete Composites* 55, 383–394. doi:10.1016/j.cemconcomp.2014.09.024

Zdeb, T. (2017). An Analysis of the Steam Curing and Autoclaving Process Parameters for Reactive Powder Concretes. *Construction Building Mater.* 131, 758–766. doi:10.1016/j.conbuildmat.2016.11.026

Zhang, J., Zhao, Y., and Li, H. (2017). Experimental Investigation and Prediction of Compressive Strength of Ultra-high Performance Concrete Containing Supplementary Cementitious Materials. *Adv. Mater. Sci. Eng.* 2017, 1–8. doi:10.1155/2017/4563164

Zhang, L., Liu, J., Liu, J., Zhang, Q., and Han, F. (2018). Effect of Steel Fiber on Flexural Toughness and Fracture Mechanics Behavior of Ultrahigh-Performance Concrete with Coarse Aggregate. *J. Mater. Civil Eng.* 30, 4018323. doi:10.1061/(ASCE)MT.1943-5533.0002519

Conflict of Interest: The authors declare that the research was conducted in the absence of any commercial or financial relationships that could be construed as a potential conflict of interest.

Publisher's Note: All claims expressed in this article are solely those of the authors and do not necessarily represent those of their affiliated organizations, or those of the publisher, the editors, and the reviewers. Any product that may be evaluated in this article, or claim that may be made by its manufacturer, is not guaranteed or endorsed by the publisher.

Copyright © 2022 Tian, Hirsch, Stephan and Lehmann. This is an open-access article distributed under the terms of the Creative Commons Attribution License (CC BY). The use, distribution or reproduction in other forums is permitted, provided the original author(s) and the copyright owner(s) are credited and that the original publication in this journal is cited, in accordance with accepted academic practice. No use, distribution or reproduction is permitted which does not comply with these terms.